11 Surface Physics

T. Greber, M. Hengsberger, J. Lobo, R. Schillinger, T. Okuda, M. Muntwiler, A. Tamai,
A. Dolocan, M. Corso, C. Cirelli, M. Morscher, L. Brandenberger, M. Klöckner, J. Osterwalder

The surface physics laboratory is well equipped for the preparation and characterization of clean surfaces, ultrathin films and nanostructures under ultrahigh vacuum (UHV) conditions. Experimental techniques available to us include x-ray photoelectron spectroscopy (XPS) and diffraction (XPD), angle-resolved photoemission spectroscopy (ARPES), two-photon photoemission (2PPE) using femtosecond laser pulses, low-energy electron diffraction (LEED) and scanning tunneling microscopy (STM). At the nearby Swiss Light Source (SLS) we operate two more photoemission spectrometers that were built in our department: a high-resolution ARPES experiment with a three-dimensional spin polarimeter for spin-resolved Fermi surface mapping (the COmplete PHotoEmission Experiment, COPHEE, stationed at the Surface and Interface Spectroscopy beamline of the SLS), and an angle-resolved XPS chamber for near-node photoelectron holography stationed at the Surface and Interface Microscopy beamline of the SLS.

The research carried out during the report period can be grouped into four topics:

- **Electronic states at metal surfaces**
  When we studied the monolayer system of Pb on Cu(111) a couple of years ago for its properties as a surfactant in thin film growth, we realized that the Pb film could be melted on the Cu(111) surface at temperatures below the onset of desorption. A unique opportunity was thus opened to study electronic states in a *liquid* layer by ARPES. The presence of the ordered Cu lattice provides the reciprocal lattice vectors needed for defined electron momentum mapping. The electron dispersion and Fermi surface mapping data described in Section 11.1 give detailed information about the character and the coherence length of the states. It is the first study of its kind and has raised a lot of interest (1). The close-packed (111) surface of gold exhibits a so-called Shockley surface state that propagates almost freely within the surface plane and thus exemplifies a two-dimensional gas of nearly-free electrons (2DEG). This is manifested in a parabolic energy dispersion relation. Due to the high atomic number of Au, this 2DEG is subject to spin-dependent momentum shifts, induced by the Rashba effect that has its origin in the spin-orbit interaction. The COPHEE spectrometer provides direct experimental access to these momentum shifts and the detailed *spin structure* in reciprocal space. Currently, we are trying to learn how such spin structures can be modified by introducing defined structural defects in the surface. Au(17 11 9) is a vicinal Au(111) surface that exhibits a regular array of steps and kinks. On this surface, the surface state spectra are much broader, but with the help of spin resolution, the Rashba-split components can still be resolved (Section 11.2). From these measurements we hope to obtain useful information about spin-dependent scattering processes at defects, and thus eventually on spin-dependent transport properties that are at the heart of the new field of *spintronics*.

- **Monolayer films of hexagonal boron nitride on metal surfaces**
  The preparation of well-defined monolayer-thick films permits us to study the structural, electronic and magnetic properties at an interface between two different materials. On Rh(111) the *h*-BNfilm self-assembles into a remarkable nanostructure in the form of a two-layer *nanomesh*, that may also be useful as a support for *functionalized surfaces*. The

mesh size of 3 nm with 2 nm holes is very interesting. The group has successfully applied for a EU grant (Three-year STREP project "NanoMesh" within the 6th Framework Programme) in which a consortium of 9 European partners are investigating the self-assembly process, alternative production routes and promising applications. A prerequisite for many applications is the *stability* of the formed mesh. In Sec. 11.3 it is demonstrated that the mesh is not only thermally stable, but that is withstands exposure to air and to liquid environments. An obvious step in this research is a screening for other systems that potentially form nanomeshes, maybe with different hole sizes and periodicities. In his diploma thesis, Martin Morscher finds that on Pd(111), boron nitride forms Moiré patterns in several domains rather than a well defined nanomesh (Section 11.4), and can thus be probably removed from the list of interesting candidate systems. The interface character of boron nitride films is best studied on Ni(111), where a commensurate (1x1) single monolayer is formed. Time-resolved 2PPE data from this interface exhibit very interesting dynamical phenomena within a time-window of a few hundred femtoseconds of a photo-excitation process (Section 11.5). An extremely strong enhancement of a well defined signal at temporal coincidence in a two-color pump-probe experiment is indicative of a *two-channel interference*.

- **Adsorbed molecules**
  Molecular monolayers offer a highly interesting route to prepare functionalized surfaces. In a dense layer, the electronic states of the individual molecules may start to interact with each other and form extended states, *molecular band states*, with new properties. On Cu(553), which is vicinal to Cu(111) and exhibits a regular array of steps with terraces in between that are roughly the size of a buckyball, C_{60} molecules form linear chains that alternate in brightness. In the one type of chains we find for the first time the pentagon bonding to the hexagonal terrace surface. ARPES data now indicate that this unusual bonding is accompanied by a very large band width of the highest occupied molecular orbital (HOMO) (Section 11.6). *Chirality* is another important aspect for molecular adsorption. Au(17 11 9) is a naturally chiral surface, i.e. there are kink sites with a chiral center. The question is whether these sites can distinguish left- and right-handed species of a chiral molecule like the aminoacid *cysteine*. Forward-scattering XPD patterns prove to be a unique indicator of chirality, because they display directly the chiral character of the molecule when single enantiomers are adsorbed, Indeed, we find distinct differences in the bonding of the two cysteine species (Section 11.7).

- **Time–resolved electron diffraction**
  The time-resolved low-energy electron diffraction (LEED) experiment, aimed at real-time investigations of *structural rearrangements* at surfaces, has been upgraded by attaching an electron energy analyzer to the vacuum chamber. At the same time, the Croissant measurement software (now commercialized by the start-up company *muntwiler+gresch*) has been implemented that is now common to all our photoemission spectrometers. This allows to measure energy distribution curves of the electrons emitted from the pulsed electron guns (Section 11.8). Effects of the space charge produced by thousands of electrons emitted from the cathode at the same time could thereby be studied in detail by taking energy spectra and by measuring the final electron pulse duration using the pinhole electron-photon pulse correlator (cf. *Annual Report 2003/04*). During the course of the year a new pulsed electron gun was designed and built up which provides a higher electron flux than the previous one while keeping the nominal electron pulse width at the sample in the range of a few picoseconds. First attempts to record time-resolved LEED images after ultrafast heating of Si(111) and In-(4x1)/Si(111) surfaces failed so far because of the low absorption coefficient of silicon for near-infrared light. First studies of the In-

(4x1)/Si(111) system, which exhibits a metal-insulator transition near 120 K, will be pursued using time-resolved photoemission. For the proof-of-principle of time-resolved LEED, C_{60}–monolayers on Cu(111) have been chosen as sample surface. These experiments are currently underway.

[1] Y. Petroff, Science 306 (2004) 2200.

11.1 Electronic structure of a two–dimensional liquid metal

in collaboration with: F. Baumberger, Department of Applied Physics, Stanford University, USA

The vast majority of models in condensed matter physics assumes translational invariance of the elementary building blocks. However, many widely used materials lack such symmetry. They are polycrystalline, amorphous or liquid. In particular, amorphous materials are of growing technological interest for their low production costs and often unique mechanical and electronic properties (1).

Developing a microscopic understanding of these properties remains a prime experimental and theoretical challenge. In a perfect crystal, the electronic wave functions can be classified as Bloch states, *i.e.* plane waves modulated by a lattice periodic function, and many macroscopic properties can be derived from the microscopic properties of the electronic wave functions. In amorphous or liquid materials this does not work. Moreover, the lack of periodicity markedly restricts the information provided by experimental probes that operate in reciprocal space. Consequently many fundamental problems of the electronic structure of liquids remain unresolved. The character of electronic wave functions in liquid metals, and especially to what extent they are itinerant or localized, has so far eluded experimental investigation.

Investigating by ARPES the behavior of a liquid monolayer of Pb supported on a crystalline Cu substrate, we could overcome these difficulties and directly track the localization of the electronic wave

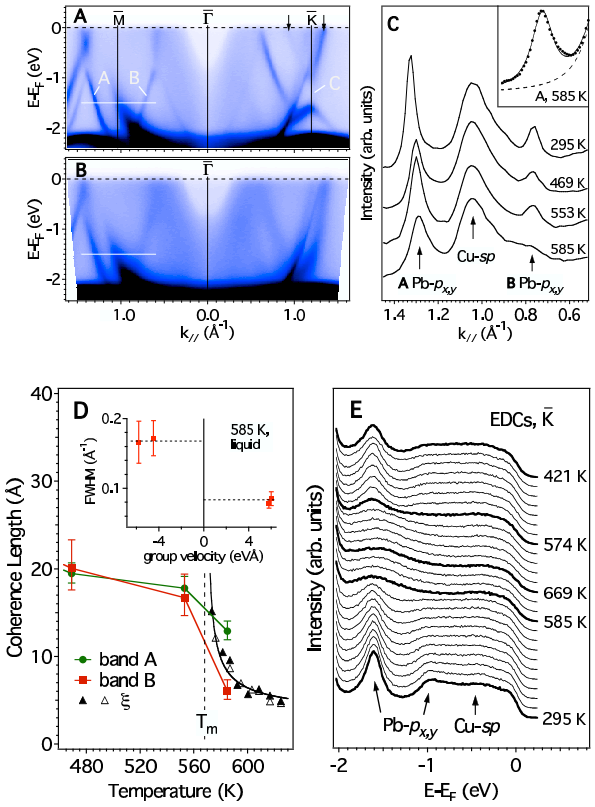

Figure 11.1:
Electron coherence in a melting lead monolayer.
A - C: ARPES data showing the measured electron dispersion and spectral function in the solid and liquid film. The Lorentzian line shape in the liquid phase indicates exponentially localized eigenstates.
D: Line widths and localization lengths are found to depend on the character of the constituting atomic wave functions.
E: Set of EDCs demonstrating the reversible filling and opening of a band gap through the phase transition (for details see Ref. [2]).

functions through the melting transition (2). It is found that states with even symmetry remain coherent over several inter–atomic distances, also well above the melting transition where the structural pair correlation length drops to only 5 – 10$\AA$ (see Fig. 11.1). Contrary, the p–like states with negative group velocity show a decay length in the liquid phase which is shorter than the wave length, *i.e.* may be considered fully localized.

[1] Physics News 689, June 21, 2004, Z.P. Lu, C.T. Liu, J.R. Thompson, and W.D. Porter, Phys. Rev. Lett. **92**, 245503 (2004).

[2] F. Baumberger, W. Auwärter, T. Greber, and J. Osterwalder, Science **306**, 2221 (2004).

11.2 Spin polarized surface states on a kinked vicinal Au(111) surface

in collaboration with:
V. N. Petrov, St. Petersburg Technical University, Russia; L. Patthey, Swiss Light Source, Paul-Scherrer Institut; and J. Henk, Max-Planck-Institut für Mikrostrukturphysik, Halle, Germany

All the noble metal (111) surfaces have an sp-derived Shockley surface state originating from the energy gap around the L-point of the bulk Brillouin zone. These states form a quasi two-dimensional electron gas (2DEG) which is confined in the direction perpendicular to the surface (1). In the case of Au(111) this surface state has been observed to be spin-split into two parabolic sub-bands, shifted in momentum with respect to each other due to the Rashba effect (1; 2; 3). The spin quantization axis is mainly contained in the surface plane, being tangent to the circular constant energy surfaces in momentum space. The sub-bands have opposite spin directions, and the circular symmetry results in zero net magnetic moment (3). In order to study the effects of steps and kinks on the generic spin structure, we have studied the related surface state on Au(17 11 9), which is a chiral surface vicinal to Au(111) with a $15.4°$ miscut angle. The surface unit cell is formed by monoatomic steps separated by $4\frac{2}{3}$ atoms, with a separation between consecutive kinks of $3\frac{1}{2}$ atoms. We observe that the surface state propagates parallel to the average surface. Compared to Au(111), it exhibits a larger electron effective mass, which is consistent with results from previously studied stepped surfaces (4). This mass enhancement is related to the scattering off the step edges. A Fermi surface map measured at room temperature, using a photon energy of 21.2 eV (He-Iα), is shown in Fig. 11.2.

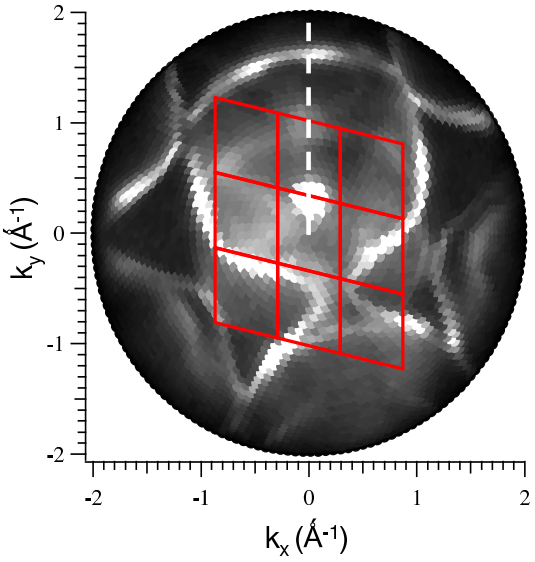

Figure 11.2:
Fermi surface map of Au(17 11 9). The red lines mark the surface Brillouin zones (BZ). The surface state is the bright spot located on the BZ boundary along the white dashed line.

The surface state is found at the boundary of the surface Brillouin zone, shifted away from normal emission in direction of the surface miscut. The binding energy of the bottom of the

surface state shifts from 470 meV in the case of Au(111) to 185 meV for Au(17 11 9). No splitting of the surface state has been found, even when measuring at high energy and angular resolution, due to the intrinsic peak broadening by the broad distribution of terrace sizes and kink separations (5).

By introducing spin resolution in ARPES, the surface state splitting into two components is again observed. These experiments were carried out at the COPHEE (COmplete PHotoEmission Experiment) end-station at the SIS beamline of the Swiss Light Source. This apparatus features two orthogonal Mott detectors which are capable of mapping the three-dimensional spin polarization vector for any value of electron momentum. In a preliminary study it has been found that the surface state spin structure is quite complex; the data are still being analysed. Some data are shown in Fig. 11.3, which represent the three orthogonal spin components along a polar scan, sampling the surface state along the dotted white line shown in the Fermi surface map of Fig. 11.2. The polarization is mainly in-plane for the surface state. The in-plane tangential component shows a Rashba-type momentum shift similar to the case of Au(111). By contrast, there is here also a contribution to the in-plane radial component, which is along the scan direction. Further experiments aimed at resolving the full picture of the surface state spin structure of Au(17 11 9) are underway.

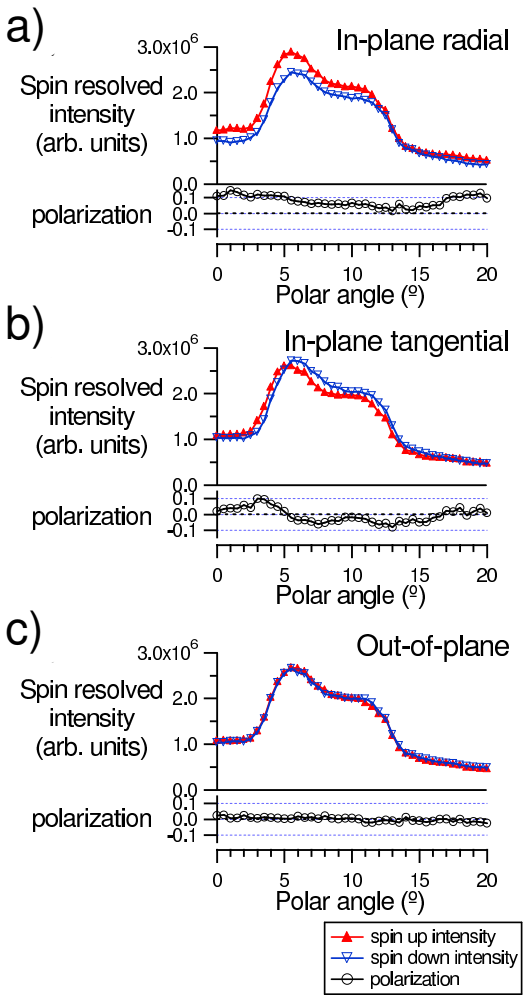

Figure 11.3:
Spin polarization and spin-resolved momentum distribution curves along the white dashed line in Fig. 11.2 for three orthogonal components of the spin polarization vector:
a) in-plane radial polarization,
b) in-plane tangential polarization, and
c) out-of plane polarization.
The scan covers $1\frac{1}{2}$ Brillouin zones.

[1] F. Reinert, G. Nicolay, S. Schmidt, D. Ehm, S. Huefner, Phys. Rev. B **63**, 115415 (2001).

[2] S. LaShell, B. A. McDougall, E. Jensen, Phys. Rev. Lett. **77**, 3419 (1996).

[3] M. Hoesch , M. Muntwiler, V. N. Petrov, M. Hengsberger, L. Patthey, M. Shi, M. Falub, T. Greber, J. Osterwalder, Phys. Rev B **69**, 241401 (2004).

[4] A. Mugarza, J. E. Ortega, J. Phys.: Condens. Matter **15**, S2381 (2003).

[5] F. Baumberger, M. Hengsberger, M. Muntwiler, M. Shi, J. Krempasky, L. Patthey, J. Osterwalder, T. Greber, Phys. Rev. Lett. **92**, 196805 (2004).

11.3 *h*–BN on Rh(111): a stable nanomesh

in collaboration with: O. Bunk, Swiss Light Source, Paul-Scherrer Institut

Recently our group has discovered a new nanostructure (Fig. 11.4a) of *h*–BN on Rh(111) (1). It appears as a two-layer mesh of *h*–BN units, with a periodicity of 3 nm and 2 nm hole size. The nanomesh self-assembles during thermal decomposition of Borazine $(HBNH)_3$ molecules on the hot Rh(111) surface. Hole formation is likely driven by the lattice mismatch of -6.7% between the film and the Rh substrate. The stability of the nanomesh in various environments is an important aspect in view of its possible applications as a template for regular nanostructures or as a functional surface for nanocatalysis or biocatalysis. For this purpose some experiments have been performed during this year in order to test the stability of the nanomesh under exposure to air and to liquids.

Concerning the first aspect, the nanomesh has been prepared in ultra-high-vacuum (UHV) and then exposed to air for 60 hours. LEED and STM images (Fig. 11.4b) show that the structure survived. A short annealing up to 950 K largely removes the contaminants (mostly H_2O, O_2, CO_2 and CO) from the surface and brings the nanomesh back to a highly ordered state. The resistance of the nanomesh to direct contact with liquids was demonstrated by simple wetting experiments. 1 μl droplets of water and of OMCTS (Octamethylcyclotetrasiloxane, $C_8H_{24}O_4Si_4$) were deposited in air on a nanomesh sample by means of a syringe (Fig. 11.4c and 11.4d). The two liquids wet the nanomesh. It can be seen macroscopically that the OMCTS spreads completely on the surface and that the water droplet has a slightly irregular shape. The angle formed by the droplets and the surface, known as contact angle θ (Fig. 11.4e), was measured in a microscope. The resulting values of θ=$51 \pm 1^\circ$ in the case of water and θ<5° for the OMCTS, both resemble the conditions of good wetting ($\theta < 90^\circ$). XPS data clearly show that the boron and nitrogen signals are still present after exposure to liquid water and OMCTS, and after a treatment in boiling (56°) aceton ($(CH_3)_2CO$). Surface

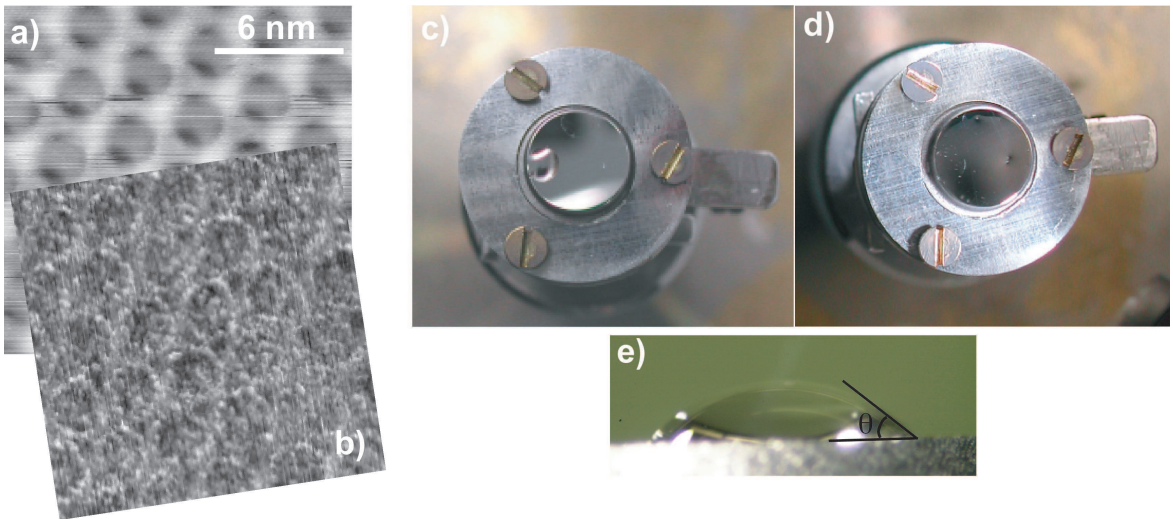

Figure 11.4:
a,b) Constant-current STM images (a: -2 V and 1.0 nA; b: -1V and 1.0 nA) of the *h*–BN nanomesh before and after air exposure ((a) and (b), respectively).
c,d) A 1 μl droplet of water (c) and OMCTS (d) placed on top of the nanomesh.
e) Microscopic side view of the water droplet in c), indicating the contact angle.

X-Ray Diffraction (SXRD) experiments at the Swiss-Light-Source confirm the stability of the *h*–BN nanomesh not only during measurements in a protective He atmosphere but also during exposure to water vapor.

[1] M. Corso, W. Auwärter, M. Muntwiler, A. Tamai, T. Greber, J. Osterwalder, Science 300 (2004) 217.

11.4 Hexagonal Boron Nitride on Pd(111) - Nanomesh or Moiré pattern?

The formation of *h*–BN layers on metal surfaces has been studied in this group for several transition metal substrates. On Ni(111), a commensurate monolayer with a slight corrugation of 0.1 Å due to the small lattice mismatch of 0.4 % is found (1). On Pd(110), several different domains of Moiré patterns are observed. The most spectacular structure is formed on Rh(111): a nanomesh where two mesh layers of boron nitride are stacked in a way to cover most of the substrate (2).
On Pd(111), the lattice mismatch of -9% also causes a coincidence lattice, but no double layer structure is observed. Instead, the boron nitride forms a flat monolayer registered to the Pd surface directions, with a second domain rotated by 30°. Additionally, *h*–BN spots are smeared out to a circle, indicating further *h*–BN domains with random orientations (Fig. 11.5 and refpdfigb). In the STM, several Moiré patterns are imaged, with periodicities ranging from 5 to 25 Å. This is consistent with the random orientations seen in the LEED, because different rotation angles create Moirés with different periodicities. The patterns can be simulated by two superimposed marble patterns with different unit lengths that are rotated against each other, which allows thus to model the STM images. Decoration experiments with C_{60} show that the top layer is flat. The bandstructure is comparable to that for *h*–BN/Ni(111), i.e. there are no strong additional sigma bands like on Rh(111) are measured. There is thus strong evidence for the absence of a double-mesh structure for *h*–BN/Pd(111).

[1] W. Auwärter, T. J. Kreutz, T. Greber, J. Osterwalder, Surf. Sci. 429 (1999) 229.
[2] M. Corso, W. Auwärter, M. Muntwiler, A. Tamai, T. Greber, J. Osterwalder, Science 303 (2004), 217.
[3] M. Corso, T. Greber, J. Osterwalder, Surf. Sci. 557 (2005), L78.

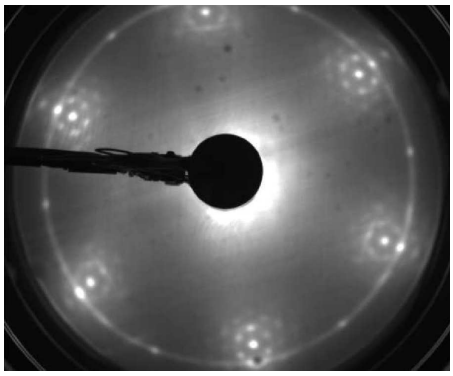

Figure 11.5:
LEED of *h*–BN/Pd(111) showing a superstructure corresponding to 11x11 *h*–BN units plus a second domain rotated by 30°. The circle is caused by azimuthally disordered *h*–BN domains.

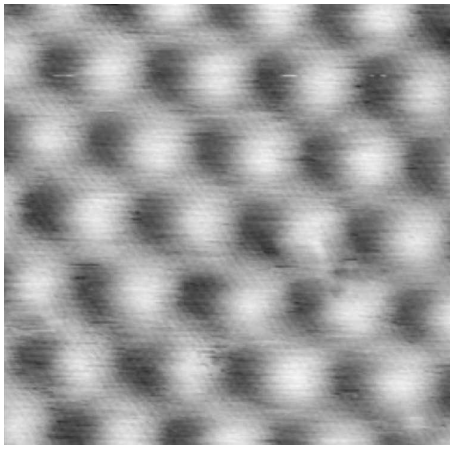

Figure 11.6:
STM image of a Moiré pattern with 27.5 Å periodicity. The apparent corrugation between the darkest and the brightest spots is 1.6 Å and is caused by the strong dependence of the tunneling current on different adsorption sites.

11.5 Time–resolved photoelectron spectroscopy from *h*-BN/Ni(1 1 1)

in collaboration with: W. Schuesslbauer and T. Ruchti, Time-Bandwidth Products AG, Technopark, 8005 Zürich, Switzerland

Deposition of *h*-BN onto Ni(1 1 1) results in atomically flat surfaces (1). The electronic properties of *h*-BN are preserved, leaving an insulating monolayer on a ferromagnetic substrate. In recent experiments, it was found that the charge transfer between the metallic substrate and C_{60} molecules deposited onto *h*-BN/Ni(1 1 1) is strongly temperature dependent: the occupancy of the lowest unoccupied state changes by a factor of seven between room temperature and about 150 K (2; 3). The underlying microscopic mechanism is related to the onset of molecular motion with increasing temperature (3) and raises new questions about the charge transport through the insulating monolayer.

Two-photon-photoemission (2PPE) is the method of choice for addressing such problems since it combines spectroscopic information about occupied and unoccupied states with real-time information about relaxation times through the use of femtosecond laser pulses (see e.g. Ref. (4) and references therein). Two different Ti:sapphire laser systems were used in these experiments: the Coherent Mira oscillator providing 800 nm pulses of 60 fs duration with a repetition rate of 76 MHz at an average power of 500 mW, and a Pallas test system (780–796 nm, 100 fs, 100 MHz, 300 mW) provided by Time-Bandwidth Products. For the time-resolved 2PPE experiments, electrons are pumped into an intermediate level by absorption of a first laser pulse and subsequently probed by excitation out of the intermediate state into the vacuum by a second, temporally delayed pulse (probe). In our case, the fundamental of 780–845 nm wavelength (about 1.55 eV) was used as pump, and its second harmonic, obtained by focusing the fundamental into 0.5–1 mm thick β-bariumborate (BBO) crystals, was used as probe.

Previous experiments, using the second harmonic for both, pump and probe, already revealed an efficient channel for optical pumping out of occupied states close to the Γ-point into a state close to the vacuum level, which was attributed to an image potential state (see Annual Report 2000/01). Furthermore, recent density-functional calculations (5) gave evidence for the existence of an unoccupied π^*-derived band within the *h*-BN–layer, roughly 1.5–1.7 eV above the Fermi level E_F. In the previous single-colour 2PPE-experiments this state showed up as small peak about 1.4 eV above E_F. It will be referred to hereafter as conduction band.

Adding fundamental light in temporal coincidence with the second harmonic changes the spectra dramatically (see Fig. 11.7): the conduction band peak shows up as a giant resonance, enhanced by orders of magnitude with respect to the peak observed without 800 nm light! There is evidence that this enhancement may be explained by resonant interaction of the two excitation channels

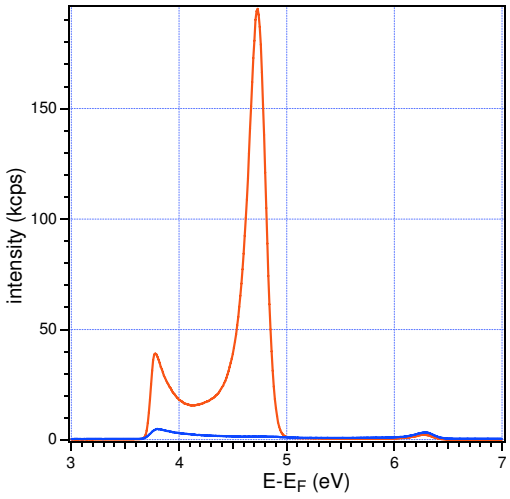

Figure 11.7:
Two-colour 2PPE experiments on *h*-BN/Ni(1 1 1): Comparison of spectra obtained by using only 400 nm light (blue curve) and pulses of 400 nm and 800 nm in temporal coincidence (red curve).

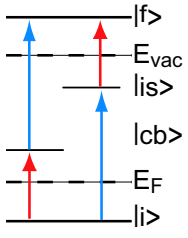

Figure 11.8:
Level scheme for the two resonating excitation channels involving four different states.

$$1: \quad |i\rangle\,(+\hbar\omega_F) \;\rightarrow |cb\rangle\,(+\hbar\omega_{SH}) \;\rightarrow |f\rangle$$
$$2: \quad |i\rangle\,(+\hbar\omega_{SH}) \;\rightarrow |is\rangle\,(+\hbar\omega_F) \;\rightarrow |f\rangle,$$

where $|cb\rangle$ and $|is\rangle$ denote the conduction band and the image state (see Fig.11.8), and ω_F and ω_{SH} the fundamental frequency and its second harmonic, respectively. $|i\rangle$ and $|f\rangle$ are the initial and final state of the excitation, which have to be identical in both interfering processes.

The temporal evolution of the intermediate state population and the dephasing time of the coherent excitations is mapped by varying the time delay between the red and blue light pulses (4), as shown in Fig.11.9. The cross-correlation curves all have an overall width of roughly 200 fs. In these curves, the location of the peak maximum depends on the kinetic energy. Likewise, strong peak shifts and changes of peak shape occur in the energy spectra during a few hundreds of femtoseconds around the time delay zero. The magnitude of this effect cannot be explained by the chirp of the light pulses because measurements at different emission angles, *i.e.* out of resonance, yield much smaller variations with energy and time delay. It is likely that the transient shifts are inherent to the resonant interaction of the two coherent excitations.

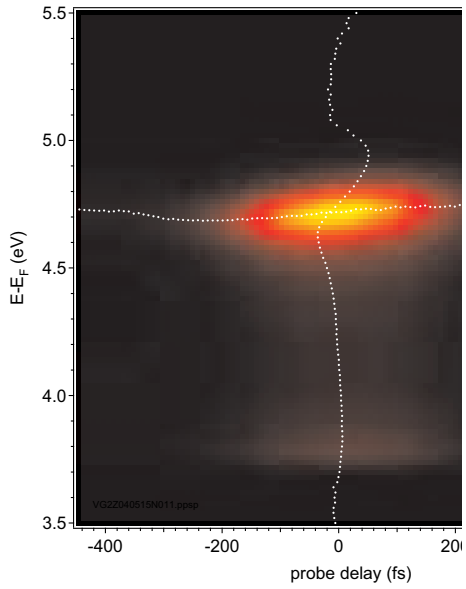

Figure 11.9:
2PPE intensity as function of energy (ordinate) above E_F and time delay of the blue with respect to the red pulse (abscissa); the peak maxima in the spectra and in the cross-correlation curve are shown as white dots.

[1] W. Auwärter, T.J. Kreutz, T. Greber, and J. Osterwalder, Surf. Sci. **429**, 229 (1999).

[2] **Nanostructured magnetic interfaces : case studies and new experiment control software**, M. Muntwiler, Ph.D. thesis, University of Zurich, 2004.

[3] M. Muntwiler, W. Auwärter, A.P. Seitsonen, J. Osterwalder, and T. Greber, Phys. Rev. B **71**, (R)121402 (2005).

[4] X.-Y. Zhu, Surf. Sci. Rep. **56**, 1 (2004).

[5] G.B. Grad, P. Blaha, K. Schwarz, W. Auwärter, and T. Greber, Phys. Rev. B **68**, 085404 (2003).

11.6 Unusually large HOMO dispersion in one-dimensional C_{60} chains

in collaboration with: A.P. Seitsonen, Physikalisch-Chemisches Institut, Universität Zürich

The fabrication of one-dimensional structures on surfaces is attracting considerable interest for possible applications in nano-electronics. Moreover, if electrons are confined to move along a single direction, these systems are expected to show novel and exotic behavior (1). C_{60} molecular chains grown on vicinal copper surfaces offer the possibility to investigate the electronic properties of one-dimensional systems where correlations and electron-lattice interactions are crucial.

In a monolayer of C_{60} on Cu(553), the molecules form long and regular double chains aligned along the step direction of the substrate (2). X-ray photoelectron diffraction data indicate that the molecules have two different and well-defined orientations: molecules adsorb either on the pentagon or on the hexagon ring. The electronic structure of this one-dimensional system has been investigated with angle resolved photoemission (ARPES). Single spectra measured at different emission angles along the C_{60} chains show significant changes in position and line shape of the highest occupied molecular orbital (HOMO) derived peak that are indicative of $\sim$400 meV band dispersion (Fig. 11.10a). In contrast, we do not observe pronounced angular dependence perpendicular to the chains, and the band width is less than 50 meV (Fig. 11.10b). The anisotropy between the two directions reveals that the electronic coupling is predominantly along the molecular chains. Interestingly, such a large HOMO dispersion has never been observed so far in solid C_{60} or in two-dimensional layers, where the reduced band width was explained with the formation of a polaron (3). Density functional theory (DFT) calculations for double molecular chains confirm a very weak coupling across the C_{60} chains (ΓX) and show a band width of 350 meV for the direction along the chains (ΓY). Quite remarkably, there is only one HOMO band, derived from C_{60} molecules sitting on the pentagon, that shows this large dispersion (blue line) and compares well with the experimental data (Fig. 11.11). This suggests that the probability to form a polaron is significantly reduced when the photohole is created in the band with higher dispersion, i.e. with a higher intermolecular hopping rate (4).

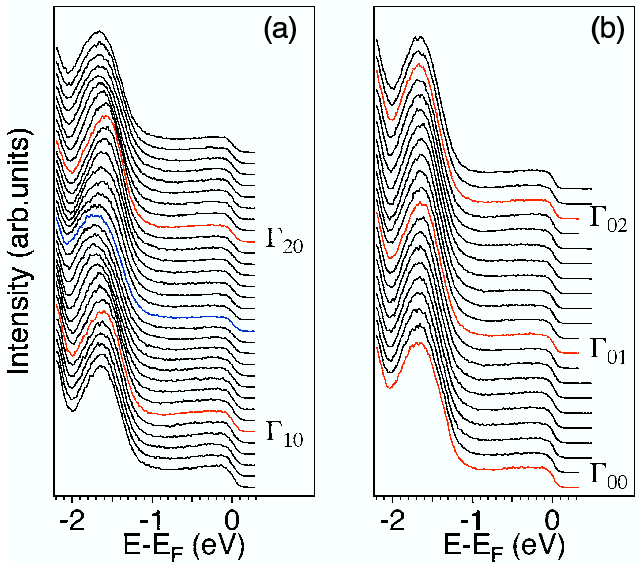

Figure 11.10:
HOMO dispersion in one-dimensional C_{60} chains. Sets of ARPES spectra measured at room temperature along an azimuthal (a) and a polar cut (b), 'parallel' and perpendicular to the chains, respectively (He Iα radiation).

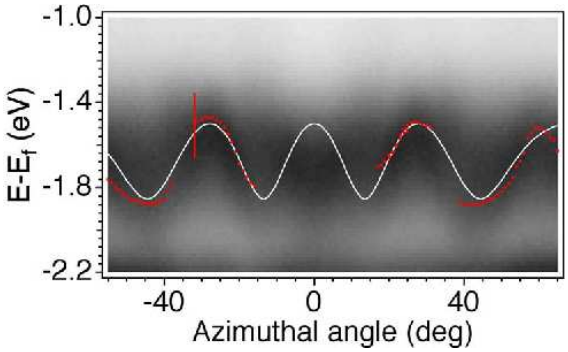

Figure 11.11:
Angular intensity distribution map. The photoemission intensity is displayed as a function of the azimuthal angle on a linear gray scale with black at maximum intensity. One HOMO band from DFT (white curve) and the peak position (red dots) as determined by a Gaussian fit to the data are superimposed.

[1] J. Voit, J. Electron Spectr. Rel. Phen. **117** (2001) 469.
[2] A. Tamai et al., Surf. Sci. **566** (2004) 633.
[3] P.A. Bruehwiler et al., Chem. Phys. Lett. **279** (1997) 85.
[4] V.R. Belosludov et al., Phys. Rev. B **67** (2003) 155410.

11.7 Chiral Heterorecognition: Cysteine on Au(17 11 9)^S

in collaboration with:
Željko Šljivančanin, École Polytechnique Fédérale de Lausanne, and Bjørk Hammer, Department of Physics and Astronomy and iNANO, University of Aarhus, Denmark

Molecular recognition is among the most fundamental processes in nature. In the lock and key model a receptor molecule discriminates a target molecule from all other molecules. For chiral recognition the receptor has to have a chiral center. If the receptor is a surface, recognition is e.g. expressed by an enantiospecific adsorption energy. First experimental evidence that chiral surfaces are enantiospecific on the molecular level came from Attard et al. who demonstrated enantioselective effects on kinked platinum surfaces (1). Near room temperature they found an effect of 13 meV in the electro-oxidation of glucose on chiral Pt(643). These small energy differences are difficult to access. A convenient twist around measuring the energy, is measuring the structure of the adsorbed enantiomers. This has been realized for homorecognition of cysteine by scanning tunneling microscopy (2) and the absolute determination of the chirality of tataric acid on Cu(110) by X-ray photoelectron diffraction (3). In both cases, however, no energy difference between the left handed and the right handed molecules is expected since these experiments were performed on non-chiral $fcc(110)$ surfaces. Here, we demonstrate that L- and D-cysteine adsorb in two distinct structures on chiral Au(17 11 9). From this it can be safely concluded that this system is enantioselective, as it was predicted for cysteine molecules where the carboxyl group is substituted with a phosphino group (4).

The experiments have been performed in a customized end-station for recording 2π X-ray photoelectron diffraction (XPD) data at the X11MA SIM beamline at the Swiss Light Source. With X-ray photoelectron spectroscopy (XPS) the molecules were identified as being in the $SC_\beta H_2 - C_\alpha H - NH_2 - COOH$ state. The coverage was determined to be below one molecule per surface unit cell ($1.08 \cdot 10^{18} \mathrm{molecules\ m}^{-2}$). Figure 11.12 shows the Au(17 11 9) unit cell and 2π X-ray photoelectron diffraction (XPD) patterns from the substrate and the adsorbates. The angular dependence of the photoemission intensities is displayed as stereographic projection using a linear grey scale (high intensities as white).

In Fig. 11.12b) the photoelectron background at 486 eV kinetic energy is shown. From the three most prominent intensity depressions along the $\langle 110 \rangle$ directions, the orientation of the

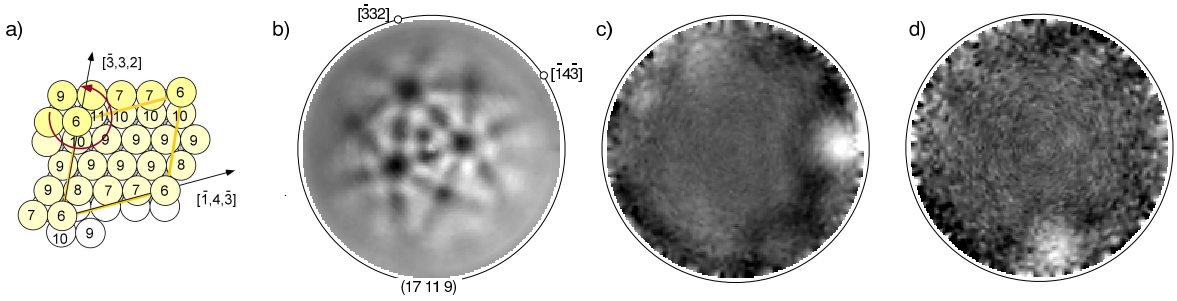

Figure 11.12:
Au (17 11 9) unit cell and angle-scanned 2π X-ray photoelectron diffraction patterns.
a) Unit cell of Au(17 11 9). The coordination numbers of the 14 surface atoms are marked.
b) Inelastic electron diffraction pattern ($E_{kin} = 486$ eV) from which the orientation and the chirality of the substrate is inferred.
c) N 1s $E_{kin} = 368$ eV emission for D-cysteine.
d) N 1s $E_{kin} = 368$ eV emission for L-cysteine.
The single forward scattering peaks in c) and d) indicate distinct single orientations for the two enantiomers.

surface and the C_1 symmetry is inferred. In Fig. 11.12 c) and d) the N 1s ($E_B = 400$ eV) emission patterns of D- and L-cysteine on Au(17 11 9) are shown. We find one dominant forward scattering maximum, though at different emission angles for L- and D-cysteine, respectively. This demonstrates two different bonding geometries and thus chiral heterorecognition or enantio-selectivity of kinks on gold. The forward scattering peaks occur at grazing angles and are identified to point along the $N - C_\alpha$ axis, where C_α is the chiral center carbon atom in cysteine. The observed structures of cysteine on Au(17 11 9) are in good agreement with those derived from density functional theory calculations.

[1] G. A. Attard, A. Ahmadi, J. Feliu, A. Rodes, E. Herrero, S. Blais, and G.Jerkiewicz, J. Phys. Chem. B, **103**, 1381 (1999).
[2] A. Kühnle, T.R. Linderoth, B. Hammer, and F. Besenbacher, Nature **415**, 891 (2002).
[3] R.Fasel, J. Wider, C. Quitmann, K.-H. Ernst and T. Greber, Angew. Chem. Int. Ed. **43**, 2853 (2004).
[4] Ž.Šljivančanin, K.V. Gothelf, and B. Hammer, J. Am. Chem. Soc. **124**, 14789 (2002) .

11.8 Time-resolved electron diffraction

in collaboration with:
H. Over, Physikalisch-Chemisches Institut, Justus-Liebig Universität Gießen, Germany

We continued the development of the time-resolved low-energy-electron diffraction (t-LEED) technique which implies the recording of LEED patterns along the time evolution of a fast surface structural change. Shortly, by hitting the sample with femtosecond laser pulses (pump), one induces fast transient modifications in the surface atomic order which are probed subsequently by means of LEED images recorded with temporally delayed electron pulses. The timescale of such processes is in the range of picoseconds. When the crystal periodicity remains unchanged on the average, the transient temperature jump gives rise to an intensity

drop of the diffraction spots due to the Debye-Waller effect. In contrast, a phase transition involving a new lattice periodicity can be seen as the (dis–) appearance of new spots in the LEED pattern. Either way the pulsed electron diffraction patterns play the role of an ultrafast thermometer, measuring the transient lattice temperature and periodicity.

11.8.1 Upgrade of the current electron gun design

For the purpose of time-resolved electron diffraction experiments, our group previously developed a laser-activated electron gun (1) which was shown to provide a pulse width below 20 ps (2). In the lens-less design of Karrer the collimation of the electrons was realized with a channelplate which results in a exceedingly small yield of electrons. Due to the small laser shot repetition rate and the low onset of space charge effects, this gun was not suited to perform an electron scattering experiment on a surface, where typically one out of 1000 electrons is scattered into the detector. Therefore a new gun design was realized with a nominal pulse width below 5 ps at 100 eV.

Particular attention was paid to minimize the solid angle occupied by the gun head in order to keep a large field of view for placing the laser pump beam and the electron detection. Furthermore, the microchannelplate used to collimate the electron beam (1) was replaced by a mesh and a lens in order to obtain maximum transmission of the gun without loss of time resolution. Figure 11.13 shows a sketch of the new electron gun head. Briefly, the cathode consists of a 20 nm thin atomically flat gold film grown on a sapphire substrate; the 400nm laser light pulses are focused from the back onto the cathode and produce electron pulses via two-photon photoemission. The electrons are then accelerated over a short distance toward a gold mesh (anode) positioned 50 μm in front of the cathode. An additional electrostatic lens is placed to focus the electrons on the sample.

The trajectories of the electrons from the cathode to the sample have been simulated (3) along the 4 mm distance. Together with the measured energy spread of 0.7 eV for 100 eV electrons, this results in a nominal time spread of less than 5 ps for a total flight time of 640 ps.

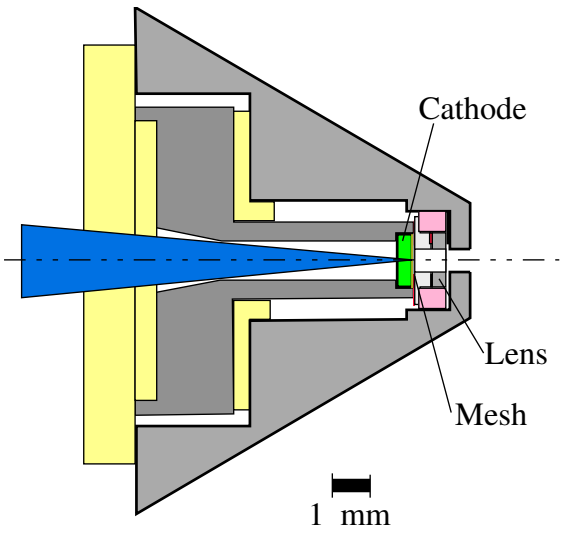

Figure 11.13:Sketch of the new electron gun.

In practice, the temporal broadening of the electron pulses (limiting the final time resolution of the t-LEED experiment) is strongly dependent on the power of the pulsed laser light hitting the cathode: the energy spectra of the electrons show a shift in energy, a broadening, and increasing asymmetry of the peak with increasing power.
This indicates the onset of effects of the large space-charge produced at the cathode within the duration of a laser pulse. The final electron current obtained at the sample position using 400 nm laser pulses of 0.5 nJ per pulse amounts to about 0.5 electrons/pulse. In comparison to the first design that provides $\mathbf{1.4 \times 10^{-4}}$ electrons/pulse for 1.2 nJ, we gain about three orders of magnitude in electron yield.

This new gun enables us to record sharp LEED patterns in a short time: in Fig. 11.14 a LEED pattern of Si(111) 7x7 is shown, obtained with an exposure time of 10 seconds at an electron kinetic energy of roughly 40 eV. The observation of most of the non-integer spots, which lie very close together in reciprocal space, is a clear indication that a well focused and collimated electron beam is sent toward the sample surface.

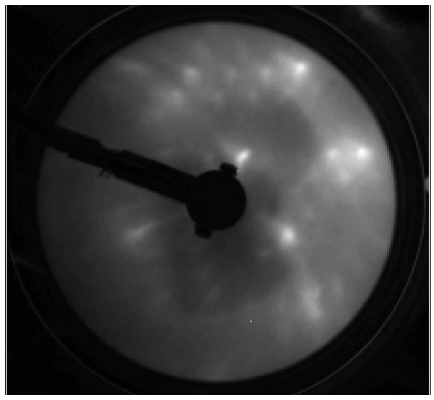

Figure 11.14:
LEED pattern of Si(111) 7x7, recorded with 40 eV electrons from the new electron gun (power 0.75 nJ/pulse, 250 kHz repetition rate, exposure time 10 seconds).

11.8.2 LEED experiments on In-(4x1)/Si(111)

For a first proof-of-principle of this new technique, a surface system exhibiting a sharp phase transition is preferable to a pure Debye-Waller effect due to the magnitude of signal change upon laser excitation. We have therefore selected a new surface system: the indium-(4x1) chain superstructure grown on Si(111) which undergoes a phase transition to an (8x2) reconstruction at about 115 K (4). Previous experiments have shown that the transition occurs within a few degrees K (4; 5), which constitutes a significant advantage of this system over recently studied surface phase transitions like that on Pb/Ge(111).
A vicinal p-doped Si(111) sample with a 2° miscut in the $(11\overline{2})$ direction was used with ohmic contacts placed along $(1\overline{1}0)$ in order to avoid step bunching during resistive heating. Well-ordered (7x7) surfaces (Fig. 11.15) were produced by fast flashes up to 1450 K for 10-15 seconds, followed by annealing at about 1120 K and slow cool down. First t-LEED data from the bare 7x7 silicon sample did not show conclusive results mainly because of the insufficient pump laser power ($\lambda = 800$ nm, 4 μJ/pulse) along with a small absorption coefficient of silicon at this wavelength.
Indium deposition at a rate of 0.05 ML/min while keeping the Si(7x7) substrate at 720 K resulted in a triple-domain (4x1) reconstruction for a $\simeq$1 ML In coverage (Fig. 11.16). The temperature dependence of the (3,3)–spot revealed a Debye temperature of about 117 K. The phase transition could not be observed so far due to bad thermal contact between sample and cryostat, which is currently being improved.

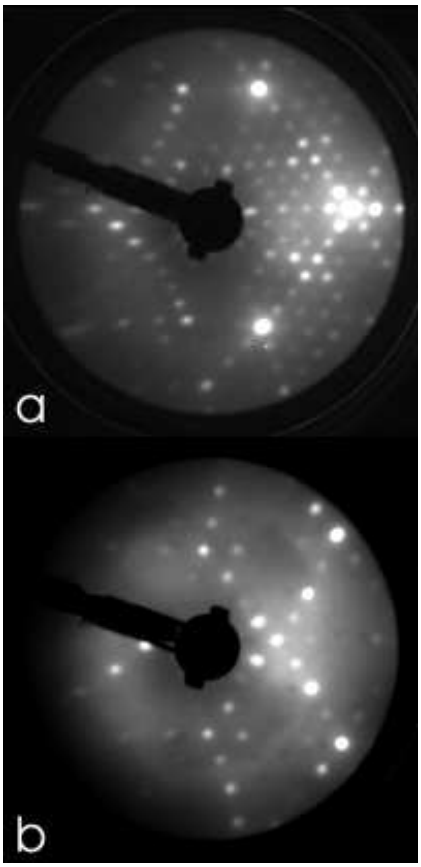

Figure 11.15:
a) LEED pattern of Si(111)-(7x7) surface collected at 66 eV electron energy. b) LEED pattern of the In-(4x1)/Si(111) superstructure at 100 eV. The two patterns were recorded with the standard LEED gun, not with the new gun described in the last section.

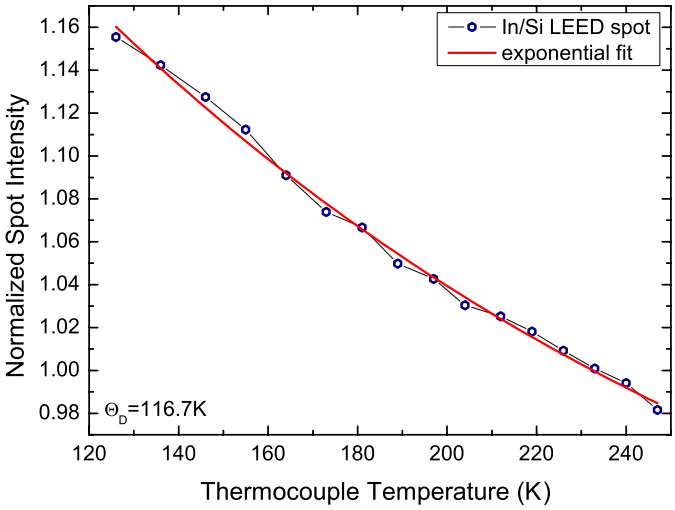

Figure 11.16:
The In-(4x1)/Si(111) (3,3) spot intensity, as a function of temperature, shows a quite low Debye temperature. The intensities were recorded at 65 eV electron energy.

[1] R. Karrer, H.J. Neff, M. Hengsberger, T. Greber, and J. Osterwalder, Rev. Sci. Instr., **72**, 4404 (2001).

[2] A. Dolocan, M. Hengsberger, H.J. Neff, M. Barry, C. Cirelli, T. Greber, and J. Osterwalder, submitted to J. Appl. Phys.

[3] SIMION software package, Idaho National Engineering Laboratory, EG&G Idaho Inc. Idaho Falls.

[4] H.W. Yeom, S. Takeda, E. Rotenberg, I. Matsuda, K. Horikoshi, J. Schaefer, C.M. Lee, S.D. Kevan, T. Ohta, T. Nagao, S. Hasegawa, Phys. Rev. Lett. **82**, 4898 (1999).

[5] O. Gallus, Th. Pillo, M. Hengsberger, P. Segovia, and Y. Baer, Eur. Phys. J. B **20**, 313 (2001).